Fall November, 2006

Snapshots of laser wakefields

Nicholas H. Matlis
Steven A. Reed
Stepan S. Bulanov
Vladimir Chvykov
Galina Kalintchenko, et al.

Snapshots of laser wakefields

N. H. MATLIS[1]*, S. REED[2], S. S. BULANOV[2], V. CHVYKOV[2], G. KALINTCHENKO[2], T. MATSUOKA[2], P. ROUSSEAU[2], V. YANOVSKY[2], A. MAKSIMCHUK[2], S. KALMYKOV[1], G. SHVETS[1] AND M. C. DOWNER[1]*

[1]FOCUS Center, Department of Physics, University of Texas at Austin, 1 University Station C1600, Austin, Texas 78712-1081, USA
[2]FOCUS Center and Center for Ultrafast Optical Science, University of Michigan, 2200 Bonisteel Blvd, Ann Arbor, Michigan 48109, USA
*e-mail: matlis@physics.utexas.edu; downer@physics.utexas.edu

Tabletop plasma accelerators can now produce GeV-range electron beams[1–5] and femtosecond X-ray pulses[6], providing compact radiation sources for medicine, nuclear engineering, materials science and high-energy physics[7]. In these accelerators, electrons surf on electric fields exceeding $100\,\mathrm{GeV\,m^{-1}}$, which is more than 1,000 times stronger than achievable in conventional accelerators. These fields are generated within plasma structures (such as Langmuir waves[8] or electron density 'bubbles'[9]) propagating near light speed behind laser[2–4] or charged-particle[5] driving pulses. Here, we demonstrate single-shot visualization of laser-wakefield accelerator structures for the first time. Our 'snapshots' capture the evolution of multiple wake periods, detect structure variations as laser–plasma parameters change, and resolve wavefront curvature; features never previously observed.

These previously invisible features underlie wave breaking, electron injection and focusing within the wake, the key determinants of charge, energy, energy spread and collimation of the accelerated beam. Because of their microscopic size and luminal velocity, these critical structures previously eluded direct single-shot observation, inhibiting progress in producing high-quality beams and in correlating beam properties with wake structure. Here, in contrast, we reconstruct wake morphology in real-time, enabling rapid feedback and optimization.

Recent advances in laser-wakefield accelerators dramatically illustrated the link between beam quality and plasma structure[1–4]. Earlier laser-wakefield accelerators produced electron beams with large divergence and energy spread, but by introducing a plasma channel guide[1,2] or by carefully adjusting the laser–plasma conditions to produce an electron density cavity behind the driving pulse[3,4], collimated, nearly mono-energetic beams from 80 MeV to 1 GeV were demonstrated. Nevertheless, the plasma structures themselves remained invisible. Previous direct measurements of laser wakes with spatial resolution better than a plasma wavelength[10–13] (λ_p) used frequency-domain interferometry[14], in which a focused femtosecond probe pulse measured local electron density $n_e(\zeta)$ at only a single time delay ζ behind the driving pulse within the co-propagating wake for each laser shot. Wake structure was then accumulated painstakingly by probing a different ζ on each subsequent shot. However, multi-shot techniques average over
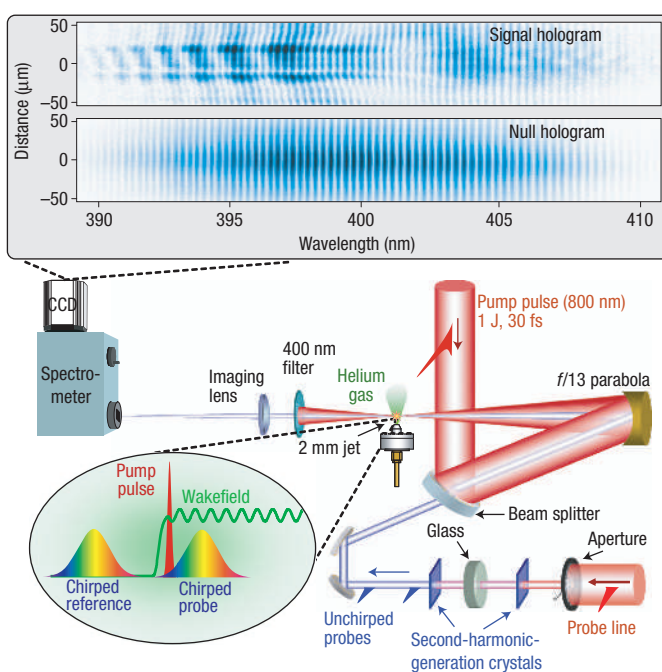

Figure 1 Experimental setup for FDH of laser wakefields. An $f/13$ parabola focuses an intense 30 fs pump pulse into a jet of helium gas, creating a plasma and laser wakefield. Two chirped, frequency-doubled 1 ps pulses, temporally synchronized and co-propagating with the pump, take holographic snapshots of the ionization front and wake. Phase alterations imposed on the trailing probe by these plasma disturbances are encoded in an FD interferogram, shown at the top with (upper) and without (lower) a pump, recorded by a charge-coupled-device camera at the detection plane of an imaging spectrometer. The wake structure is recovered by Fourier-transforming this data.

(often substantial) shot-to-shot variations of the laser-generated plasma structure, and do not provide rapid or accurate feedback for optimizing experimental parameters. Here, in contrast, we use
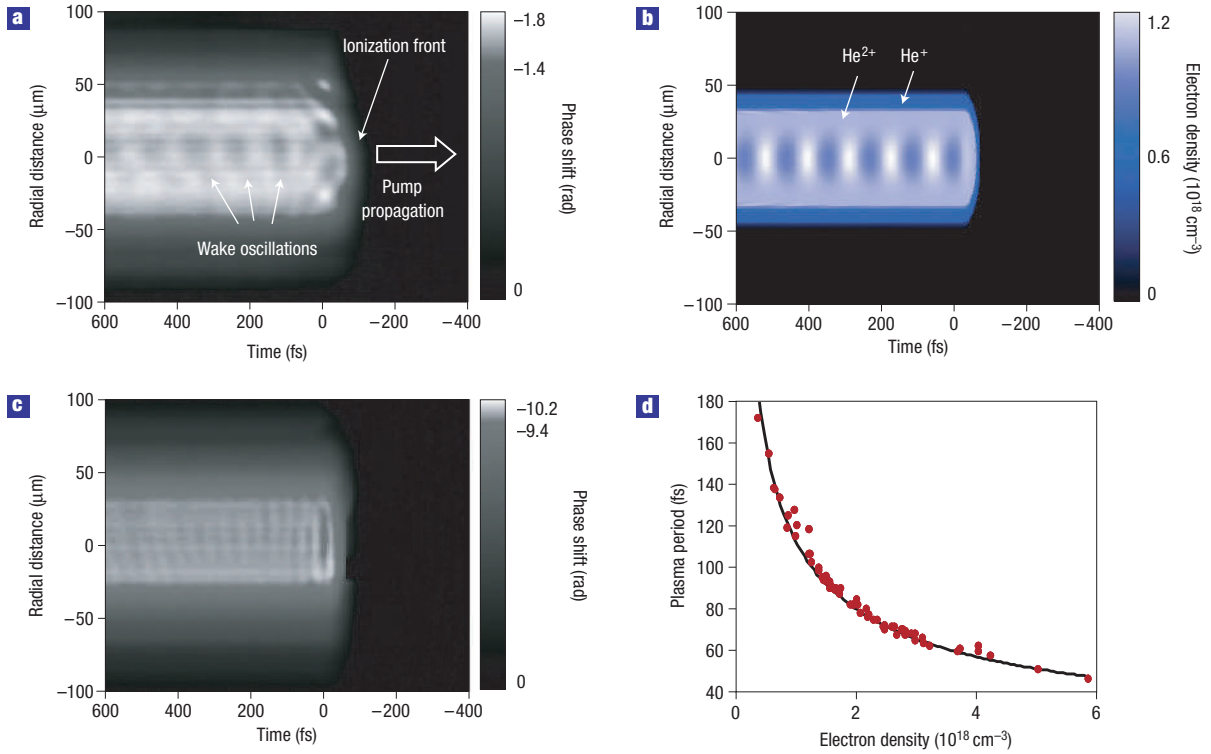
749

Figure 2 Small-amplitude wakes with flat wavefronts. a, Probe phase-shift profile $\Delta\phi_{pr}(r, \zeta)$ produced by an ~10 TW, 30 fs pump centred at zero on the horizontal scale, electron density $\bar{n}_e^{max} = 0.95 \times 10^{18}$ cm^{-3} in the He^{2+} region. **b**, Simulated wake density profile $n_e(r, \zeta)$ near the jet centre produced by an 11 TW linearly polarized pump. **c**, Same as in **a**, but $\bar{n}_e^{max} = 5.9 \times 10^{18}$ cm^{-3}. **d**, Wake period versus $\bar{n}_e^{max}$, compared with theoretical curve.

frequency-domain holography (FDH)[15], a technique designed to image structures propagating near light speed c. FDH uses a long, wide probe pulse that illuminates the entire object $n_e(r, \zeta)$ at once, like the 'object' beam of conventional holography. Here, r denotes distance from the laser propagation axis. Interference of this probe with an equally extended 'reference' pulse on a detector encodes the object's phase structure, which is subsequently 'read' to reconstruct the object, completing the analogy with conventional holography.

In our experiments, wakefields were created by focusing a ~1 J, 800 nm, 30 fs pulse from the University of Michigan's HERCULES laser system[16] into a supersonic He gas jet (see Fig. 1). Approximately 10% of the energy of each laser pulse was split off for probe pulses. A fraction of the latter was configured into a Mach–Zehnder interferometer (not shown) that probed the pump-produced plasma transversely[17], measuring its length ($L \sim 2$ mm), radius (~50 μm) and time-averaged electron density $0.5 \leq \bar{n}_e(z) \leq 6 \times 10^{18}$ cm^{-3} at each point $0 < z < L$ along the propagation path, where z denotes distance from the gas jet entrance. Wake structures the size of a plasma wavelength $15 \leq \lambda_p \leq 30$ μm, however, were not resolved by transverse probing because they propagate more than λ_p during the transit time of the probe across the interaction region.

To resolve such structures, we constructed a longitudinal probe line (see Fig. 1) that produced two co-propagating, 1 ps, linearly chirped second-harmonic pulses separated by $\Delta\tau = 3$ ps (see the Methods section). The leading pulse (centre wavelength $\lambda_{ref} = 400$ nm) arrived at the jet before the pump, and acted as a reference. The trailing pulse (hereafter 'probe', wavelength $\lambda_{pr} = 400$ nm, frequency $\omega_{pr} = 2\pi c/\lambda_{pr}$) rode with the pump, overlapping its co-propagating ionization front and wake oscillations at plasma frequency $\omega_p = (4\pi n_e e^2/\gamma m)^{1/2}$ (where

$\gamma = (1 - v^2/c^2)^{1/2}$ is the relativistic Lorentz factor, and e, m and v are the electron charge, rest mass, and oscillation velocity, respectively), which imparted time/frequency-dependent phase shifts to it. These shifts were recorded in frequency-domain (FD) fringes of period[14] $2\pi/\Delta\tau$ formed via interference of the probe and reference at the detection plane of an imaging spectrometer. Transverse spatial variations were recorded by imaging the interaction plane onto the spectrometer slit, which selected a one-dimensional lineout. The complete two-dimensional FD 'hologram' (see Fig. 1, top) encoded longitudinal (that is, temporal) phase variations along the wavelength axis and transverse spatial variations along the orthogonal (slit) axis (measurement resolution is discussed in the Methods section).

Fourier transformation of the FD hologram, analogous to 'reading' a conventional hologram with a single-frequency sine wave, recovered probe temporal phase shift[15,18] $\Delta\phi_{pr}(r, \zeta)$, which a small computer reconstructed and displayed within ~1 s. $\Delta\phi_{pr}(r, \zeta)$ is related to the plasma refractive index $\eta(r, \zeta, z) = [1 - \omega_p^2(r, \zeta, z)/\omega_{pr}^2]^{1/2}$ by

$$\Delta\phi_{pr}(r, \zeta) = \frac{2\pi}{\lambda_{pr}} \int_0^L [1 - \eta(r, \zeta, z)]dz, \quad (1)$$

which simplifies to $2\pi[1 - \eta(r, \zeta)]L/\lambda_{pr}$ for uniform $\bar{n}_e(z)$ and pump excitation. Approximating $\eta \approx 1 - \omega_p^2/2\omega_{pr}^2$ for our tenuous plasma, measured $\Delta\phi_{pr}(r, \zeta)$ and wake density profile $n_e(r, \zeta, z)$ are related by $\Delta\phi_{pr}(r, \zeta) = (e^2\lambda_{pr}/mc^2)\int_0^L[n_e(r, \zeta, z)/\gamma(r, \zeta, z)]dz \approx e^2\lambda_{pr}Ln_e(r, \zeta)/\gamma(r, \zeta)mc^2$ for non-uniform and uniform plasma, respectively. Single-shot FDH reconstruction of ionization fronts generated by low-intensity pump pulses was demonstrated previously[15,18], but not wakes generated by relativistic laser–plasma interaction. For the latter,
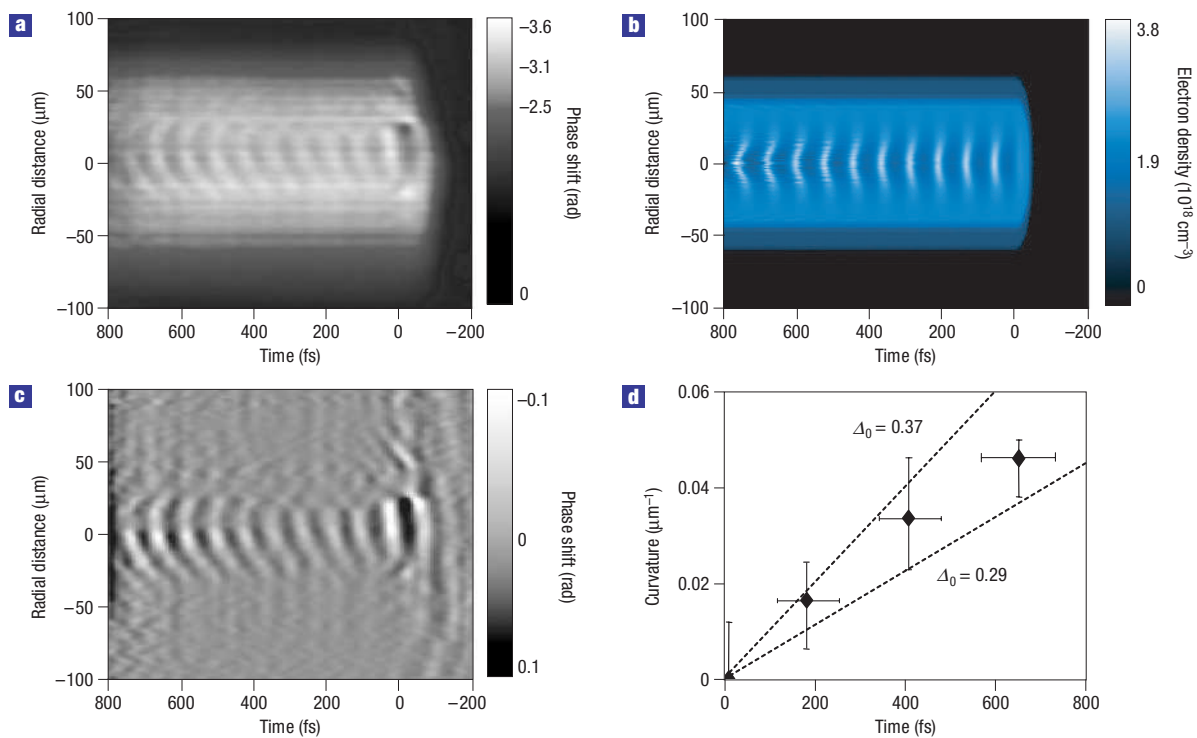
Figure 3 Strongly driven wake with curved wavefronts. **a**, Probe phase profile $\Delta\phi_{pr}(r, \zeta)$ for an ~30 TW pump, $\bar{n}_e^{max} = 2.2 \times 10^{18}$ cm^{-3} in the He^{2+} region. **b**, Simulated density profile $n_e(r, \zeta)$ near the jet centre. **c**, Same data as in **a**, with the background $\bar{n}_e$ subtracted to highlight the wake. **d**, Evolution of the reciprocal radius of wavefront curvature behind the pump (data points), compared with calculated evolution (dashed lines) for indicated wake potential amplitudes. Each data point (except at $\zeta = 0$) averages over three adjacent periods. The horizontal error bars extend over the three periods averaged, and the vertical error bars extend over the range of fitted curvature values averaged.

scattered pump light must be carefully excluded from the FD holograms, a task we accomplish by using frequency-doubled probe and reference pulses[15]. For $\bar{n}_e \lesssim 10^{19}$ cm^{-3}, complete frequency discrimination was achieved without difficulty. For $\bar{n}_e \gtrsim 10^{19}$ cm^{-3}, the pump-generated supercontinuum extended to 400 nm, introducing weak background fringes, whereas the group-velocity walkoff between the 400 nm probe-reference pulses and plasma structures, which propagate at a phase velocity equal to the pump group velocity[8], began to degrade the longitudinal resolution. Although straightforward improvements to FDH (see the Methods section) should overcome such difficulties, here we report results for $\bar{n}_e \leq 6 \times 10^{18}$ cm^{-3} where they do not arise.

Figure 2a,c shows reconstructed images of wakes produced in a jet with a backing pressure of (a) 26 kPa (200 torr) or (c) 93 kPa (700 torr) by pump pulses of peak power ~10 TW and vacuum-focused intensity ~10^{18} W cm^{-2}. In both images, a sharp ionization front is observed in the leading edge of the pump, and a He^{2+} plateau and surrounding He$^+$ corona in its wake. The latter are identified by a sharp discontinuity in n_e at their boundary ($|r| \approx 35$ μm), where pump intensity drops to the field ionization threshold[19] (~10^{16} W cm^{-2}) for He$^+$. In the He^{2+} cores of Fig. 2, either 5 (Fig. 2a) or 14 (Fig. 2c) periods of sinusoidal oscillations of wavelength $\lambda_p = 35$ μm (Fig. 2a) or 13.5 μm (Fig. 2c), with nearly flat wavefronts, are clearly observed. To help understand this result, we simulated ionization and wake generation using the particle-in-cell code WAKE[20] in an axisymmetric geometry, assuming a pump pulse with a gaussian radial and temporal profile focused at the gas jet entrance, using the density profile $\bar{n}_e(z)$ measured by the transverse interferometer. Our simulations indeed predict flat wavefronts for these laser–plasma parameters.

For example, Fig. 2b shows simulated ionization fronts and wake generated by an 11 TW pulse near the jet centre, where He^{2+} density reaches its maximum value $\bar{n}_e^{max} = 0.95 \times 10^{18}$ cm^{-3}, as in Fig. 2a. Simulated and measured wake oscillation periods T_{wake} agree exactly. In addition, the radial extents of the He^{2+} core and wake oscillations agree closely. The measured He$^+$ sheath is wider than the simulated one and varies from shot-to-shot, probably because of fluctuating non-gaussian radial wings and scattering of the pump pulse. As plasma oscillates at ω_p behind the pump, $T_{wake} = 2\pi/\omega_p$ is expected[8]. We observe $T_{wake} = 2\pi/\omega_p^{max}$, where $\omega_p^{max} = (4\pi\bar{n}_e^{max}e^2/\gamma m)^{1/2}$, on every shot, as shown in Fig. 2d for several dozen shots. The agreement is excellent, despite using no fitting parameters, and suggests that the main features of $\Delta\phi_{pr}(r, \zeta)$ are determined in the densest portion of the $\bar{n}_e(z)$ profile.

Figure 3a shows the ionization front and wake produced by an ~30 TW laser pulse. This wake has curved wavefronts, a clear signature of strongly driven, nonlinear laser–plasma interaction[21–24]. The wavefronts evolve from flat profiles immediately behind the pump to curved 'horse-shoe' profiles after several periods. A simulated wake driven by a 35 TW pump focused to $1/e^2$ intensity radius $r_0 = 25$ μm, shown in Fig. 3b, best reproduces the degree of curvature, its rate of change behind the drive pulse, and the relative widths of wake and ionized He. To highlight wavefront curvature, Fig. 3c shows the same wake as in Fig. 3a after subtracting the phase shift from the index change due to the background plasma. The data points plotted in Fig. 3d show the evolution of the reciprocal wavefront radius $\rho^{-1}(\zeta)$, obtained by fitting the wavefronts within $r < r_0$ to circular arcs. Such curvature, though simulated with nonlinear fluid[22] and particle[21,23] codes, has never previously been observed in the laboratory.
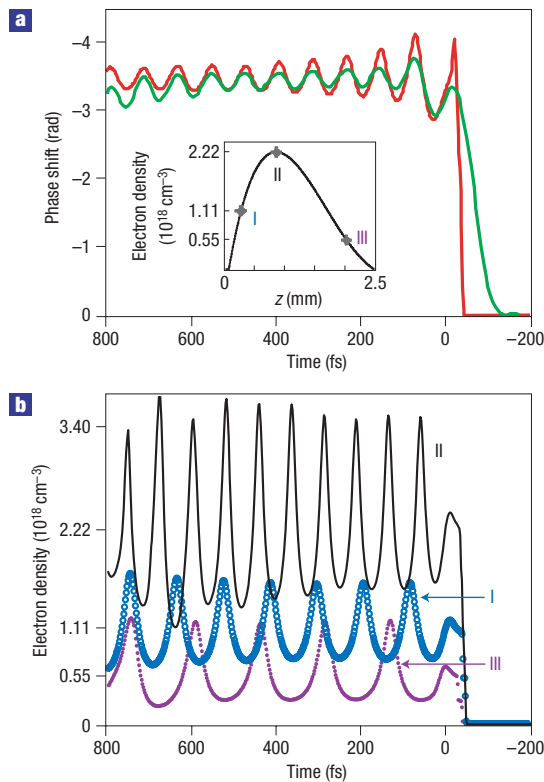
Figure 4 Axial lineouts of ionization front and wake oscillations. a, Measured (green curve) and simulated (red curve) probe phase shift $\Delta\phi_{pr}(r=0,\zeta)$. Inset: Time-averaged plasma profile $\bar{n}_e(z)$ of the gas jet measured by transverse interferometry. **b,** Simulated wake oscillations $\delta n_e/n_e(r=0,\zeta)$ at the three locations in the jet—I (blue curve) before peak; II (black curve) at peak; III (purple curve) after peak—as indicated in the inset of **a**, showing variation in amplitude and frequency.

The wavefront curves because, as the plasma wave amplitude $\delta_0 \equiv |\delta n_e(r=0)/n_e|_{max}$ approaches unity on the axis, the electrons making up the wave oscillate relativistically ($\gamma > 1$), causing $\omega_p(r=0)$ to decrease by $\sqrt{\gamma}$ relative to its off-axis value[21,22]. Thus, $\rho^{-1}(\zeta)$ depends sensitively on δ_0; for weakly relativistic ($\gamma \lesssim 2$) wakes, simulations are consistent with the analytic approximation[24] $\rho^{-1}(\zeta) \approx 0.45\zeta[\Delta_0/r_0]^2$, with ρ and r_0 in micrometres and ζ in femtoseconds. Here Δ_0 is the amplitude of oscillations in the electrostatic wake potential (normalized to mc^2/e), from which δ_0 is determined exactly ($\delta_0 \to \Delta_0$ for small δ_0)[22]. FDH measurement of $\rho(\zeta)$ thus determines the peak amplitude of the nonlinear wake. This is illustrated by the theoretical curves in Fig. 3d, showing simulated $\rho^{-1}(\zeta)$ for $\Delta_0 = 0.29$ and 0.37, $r_0 = 25\,\mu m$, which bound the experimental values. $\Delta_0 = 0.33 \pm 0.04$ (hence $\delta_0 \approx 0.5$) is thus consistent with the data. Curvature is important because of its role in electron injection[2–4], wave-breaking[21,23], and focusing[22,24] of accelerated electrons. Supplementary Information, Fig. S1 shows wake reconstructions for a variety of laser–plasma conditions.

In Fig. 4, oscillation amplitudes, indicated heretofore by grey scales, are plotted quantitatively. The red curve in Fig. 4a shows simulated $\Delta\phi_{pr}(r=0,\zeta)$ for the wake in Fig. 3, using the longitudinal density profile $\bar{n}_e(z)$ measured by transverse interferometry (see Fig. 4a, inset). It agrees well with the measured $\Delta\phi_{pr}(r=0,\zeta)$ (green curve), an axial lineout of Fig. 3a. As $\bar{n}_e(z)$ is non-uniform, the amplitude of these $\Delta\phi_{pr}$ oscillations is

related to δ_0 by the integral equation (1)—that is, the curves in Fig. 4a are longitudinal averages of wakes of varying amplitude and frequency, as shown in Fig. 4b. The strongest, highest frequency wakes (see curve II, an axial lineout of Fig. 3b), concentrated near the jet centre, determine the main features of $\Delta\phi_{pr}(r,\zeta)$. Weaker, lower frequency wakes (curves I, III) from graded density regions round off sharp $\Delta\phi_{pr}$ features accumulated in the centre. Finite probe bandwidth also contributes to this rounding. The use of wider bandwidth probes will eliminate the latter contribution, but not the effects of non-uniform $\bar{n}_e(z)$. Nevertheless, our simulations show that the frequency, curvature and amplitude of the oscillatory component of $n_e(r,\zeta)$ near the centre of the jet are well approximated by $mc\omega_{pr}\Delta\phi_{pr}(r,\zeta)/2\pi e^2 L_{eff}$, where $L_{eff} \approx 1.5\,mm$ is an effective interaction length in which Δ_0 is maximum. With guidance from simulations, L_{eff} can be re-evaluated for other laser–plasma conditions. Such algorithms for inverting $\Delta\phi_{pr}(r,\zeta)$ to approximate z-dependent $n_e(r,\zeta,z)$ are analogous to standard Abel inversions of transverse interferograms to approximate r-dependent density profiles of cylindrical plasma columns[25]. In future experiments, such approximations can be eliminated by probing wakes in sharply bounded uniform plasmas produced by truncating non-uniform regions with a machining laser[26]. $\Delta\phi(r,\zeta)$ and $n_e(r,\zeta)$ are then related simply by a multiplicative constant. Even in the current longitudinally averaged FDH configuration, however, wavefront curvature independently measured wake amplitude.

The ability to capture detailed snapshots of elusive luminal-velocity plasma structures opens a direct window into the microscopic physics of relativistic laser–plasma interactions, and is an essential step towards controlling them. Much as copper structures must be micro-engineered to optimize radiofrequency accelerators, plasma wakes, rendered visible, could be sculpted in real-time using FDH in combination with high-speed simulations, feedback-controlled drive pulse parameters and electron beam characterization. Direct observation of the dynamic interplay among driving pulse, plasma wave and accelerated electrons—including beam loading, wave-breaking and pump depletion—will be essential for realizing potential applications[7] of plasma accelerators to, for example, radiobiology, radiotherapy, radiographic materials inspection, ultrafast chemistry and high-energy physics.

METHODS

LASER

The HERCULES laser system produced ultrashort ultraintense laser pulses by chirped-pulse amplification, using titanium-doped sapphire gain media. The uncompressed beam was split 90–10 into pump and probe beams, which were then independently compressed to 30 fs. An $f/13$ parabola focused the pump beam into the gas jet. The reference-probe pulse sequence was created as follows (see Fig. 1): first, the input 800 nm probe pulse up-converted to 400 nm in a thin (200 μm) potassium dihydrogen phosphate crystal; the remaining, nearly undepleted 800 and 400 nm pulses then passed through a half-inch of glass, in which they separated temporally via group-velocity dispersion; the temporally advanced 800 nm pulse then up-converted in an identical potassium dihydrogen phosphate crystal, generating a second 400 nm pulse collinear with the first, and advanced in time by ~3 ps. These pulses recombined collinearly with the pump through a 1-inch-thick high reflector for 800 nm with high transmission at 400 nm, which chirped and stretched them to ~1 ps duration via linear dispersion, establishing the temporal window that FDH sampled.

ANALYSIS OF FD HOLOGRAMS

A LabVIEW analysis program running on a personal computer acquired data, and reconstructed and displayed wake structure. Each FD hologram was analysed by reconstructing the probe's electric field

$E_{pr}(r,\omega) = |E(r,\omega)|e^{i\phi(r,\omega)}$ (where $\phi(r,\omega) = \phi_{chirp}(r,\omega) + \Delta\phi(r,\omega)$) in the spectral domain, then Fourier-transforming to the time-domain to recover the temporal phase perturbation $\Delta\phi_{pr}(r,\zeta)$, from which the wake electron-density profile $n_e(r,\zeta)$ is derived. Chirp phase $\phi_{chirp}(r,\omega)$ is measured independently. The wake-modulated probe amplitude $|E(r,\omega)|$ and spectral phase change $\Delta\phi(r,\omega)$ are recovered from Fourier analysis of the hologram. Transverse spatial resolution was measured by recording images of calibrated micrometre-scale test structures, which confirmed that it was close to the theoretical limit $f^{no.}\lambda_{ref} \sim 3\,\mu m$ set by the f-number of the imaging optics ($f^{no.} \approx 8$), which provided threefold magnification. To first order, temporal resolution behind the pump is the reciprocal reference bandwidth $\Delta t_{res} \approx 2\pi/\Delta\omega_{ref} \approx 30\,fs$, as confirmed by test FDH measurements of optical-Kerr-effect phase shifts in glass induced by femtosecond pump pulses of calibrated duration[15,18]. Nonlinearity of the probe and reference chirp[18] and detector noise[14] can introduce additional second-order corrections. At densities $\bar{n}_e > 10^{19}\,cm^{-3}$, the walk-off between the 400 nm probes and plasma structures propagating at the 800 nm pump group velocity began to degrade the longitudinal resolution. We anticipate that the use of laser machining to truncate plasma interaction length[26] and probe-reference pulses closer in wavelength to the pump will reduce this effect.

Also at $\bar{n}_e > 10^{19}\,cm^{-3}$, the pump-generated supercontinuum at 400 nm began to introduce background fringes at periods $2\pi/\Delta\tau_{pu-ref}$ and $2\pi/\Delta\tau_{pu-pr}$, corresponding to reciprocal pump–reference and pump–probe time separations, respectively, thus complicating reconstruction. We anticipate that the use of more intense probe-reference pulses (to render the background insignificant), improved polarization discrimination of the probes from the pump, and Fourier filtering of background fringes before analysis of FD holograms will effectively suppress such artefacts.

SIMULATIONS

The code WAKE is a fully relativistic particle-in-cell code that can be used in two-dimensional planar or three-dimensional axisymmetric geometry. It calculates the quasistatic plasma response to the ponderomotive force averaged over the laser period and to the self-consistent electric and magnetic fields of the plasma wake. Propagation of the linearly polarized laser beams is described in the extended paraxial approximation. The code calculates precisely the linear group velocity of both 800 nm pump and 400 nm probe-reference pulses. Optical field (tunnelling) ionization of neutral gas is included. The simulations presented here used grid size $\Delta x = \Delta r = 0.16 k_p^{-1}$, 15 particles per cell, and a moving window 4.5 ps long and $\sim 100\,\mu m$ wide. The technique originally designed for modelling multi-shot frequency-domain interferometry[11] was adapted for FDH simulations.

References

1. Leemans, W. P. et al. GeV electron beams from a centimetre-scale accelerator. *Nature Phys.* **2**, 696–699 (2006).
2. Geddes, C. et al. High-quality electron beams from a laser wakefield accelerator using plasma-channel guiding. *Nature* **431**, 538–541 (2004).
3. Mangles, S. et al. Monoenergetic beams of relativistic electrons from intense laser–plasma interactions. *Nature* **431**, 535–538 (2004).
4. Faure, J. et al. A laser–plasma accelerator producing monoenergetic electron beams. *Nature* **431**, 541–544 (2004).
5. Hogan, M. J. et al. Multi-GeV energy gain in a plasma-wakefield accelerator. *Phys. Rev. Lett.* **95**, 054802 (2005).
6. Rousse, A. et al. Production of a keV X-ray beam from synchrotron radiation in relativistic laser–plasma interaction. *Phys. Rev. Lett.* **93**, 135005 (2004).
7. Malka, V., Faure, J., Glinec, Y. & Lifschitz, A. F. Laser plasma accelerators: a new tool for science and for the society. *Plasma Phys. Control. Fusion* **47**, B481–B490 (2005).
8. Tajima, T. & Dawson, J. M. A laser plasma accelerator. *Phys. Rev. Lett.* **43**, 267–270 (1979).
9. Pukhov, A. & Meyer-ter-Vehn, J. Laser wakefield acceleration: the highly nonlinear broken-wave regime. *Appl. Phys. B* **74**, 355–361 (2002).
10. Siders, C. W. et al. Laser wakefield excitation and measurement by femtosecond longitudinal interferometry. *Phys. Rev. Lett.* **76**, 3570–3573 (1996).
11. Marques, J.-R. et al. Laser wakefield: experimental studies of nonlinear radial oscillations. *Phys. Plasmas* **10**, 1124–1134 (1998).
12. Takahashi, E. et al. Observation of spatial asymmetry of THz oscillating electron plasma wave in a laser wakefield. *Phys. Rev. E* **62**, 7247–7250 (2000).
13. Kotaki, H. et al. Direct measurement of coherent ultrahigh wakefields excited by intense ultrashort laser pulses in a gas-jet plasma. *Phys. Plasmas* **9**, 1392–1400 (2002).
14. Geindre, J. P. et al. Frequency-domain interferometer for measuring the phase and amplitude of a femtosecond pulse probing a laser-produced plasma. *Opt. Lett.* **19**, 1997–1999 (1994).
15. Le Blanc, S. P., Gaul, E. W., Matlis, N. H., Rundquist, A. & Downer, M. C. Single-shot ultrafast phase measurement by frequency domain holography. *Opt. Lett.* **25**, 764–766 (2000).
16. Bahk, S.-W. et al. Generation and characterization of the highest laser intensities. ($10^{22}\,W\,cm^{-2}$). *Opt. Lett.* **29**, 2837–2839 (2004).
17. Chen, S.-Y., Sarkisov, G. S., Maksimchuk, A., Wagner, R. & Umstadter, D. Evolution of a plasma waveguide created during relativistic ponderomotive self-channeling of an intense laser pulse. *Phys. Rev. Lett.* **80**, 2610–2613 (1998).
18. Kim, K. Y., Alexeev, I. & Milchberg, H. M. Single-shot supercontinuum spectral interferometry. *Appl. Phys. Lett.* **81**, 4124–4126 (2002).
19. Augst, S., Meyerhofer, D. D., Strickland, D. & Chin, S. L. Laser ionization of noble gases by Coulomb-barrier suppression. *J. Opt. Soc. Am. B* **8**, 858–867 (1991).
20. Mora, P. & Antonsen, T. M. Jr. Kinetic modeling of intense, short laser pulses propagating in tenuous plasmas. *Phys. Plasmas* **4**, 217–229 (1997).
21. Bulanov, S. V., Pegoraro, F., Pukhov, A. M. & Sakharov, A. S. Transverse-wake wave breaking. *Phys. Rev. Lett.* **78**, 4205–4208 (1997).
22. Andreev, N. E., Gorbunov, L. M. & Ramazashvili, R. R. Theory of a three-dimensional plasma wave excited by a high-intensity laser pulse in an underdense plasma. *Plasma Phys. Rep.* **23**, 277–284 (1997).
23. Decker, C. D., Mori, W. B. & Katsouleas, T. Particle-in-cell simulations of Raman forward scattering from short-pulse high-intensity lasers. *Phys. Rev. E* **50**, R3338–R3341 (1994).
24. Kalmykov, S., Gorbunov, L. M., Mora, P. & Shvets, G. *12th Advanced Accelerator Concepts Workshop, Lake Geneva, Wisconsin, 2006.* AIP Proc. (in the press).
25. Pretzler, G., Jäger, H., Neger, T., Philipp, H. & Woisetschläger, J. Comparison of different methods of Abel inversion using computer-simulated and experimental side-on data. *Z. Naturf. A* **47**, 955–970 (1992).
26. Pai, C.-H. et al. Fabrication of spatial transient-density structures as high-field plasma photonic devices. *Phys. Plasmas* **12**, 070707 (2005).

Author contributions

N.H.M. designed and set up the experiment and data acquisition system and acquired and analysed all data presented, with assistance from S.R. A.M. supervised the experiments on site. V.Y. supervised construction and operation of the HERCULES laser system, and V.C. and G.K. operated it during the experiments. P.R. assisted with characterization of laser pulses and computerized data acquisition. T.M. provided a key insight in configuring the chirped probe pulses. S.K. and G.S. carried out all WAKE simulations presented in the paper, and S.S.B. confirmed them independently with a separate code and contributed to theoretical interpretation. M.C.D. conceived and co-supervised the experiment, and wrote the paper. All authors discussed the results and commented on the manuscript.

Competing financial interests

The authors declare that they have no competing financial interests.

Reprints and permission information is available online at http://npg.nature.com/reprintsandpermissions/